applied sciences

MDPI

Article

Electronic Properties of Electron-Deficient Zn(II) Porphyrins for HBr Splitting

Serena Berardi [1,*], Stefano Caramori [1], Elisabetta Benazzi [1], Nico Zabini [1], Alessandro Niorettini [1], Alessio Orbelli Biroli [2], Maddalena Pizzotti [3], Francesca Tessore [3,*] and Gabriele Di Carlo [3]

1 Department of Chemical and Pharmaceutical Sciences, University of Ferrara, Via Luigi Borsari 46, 44121 Ferrara, Italy
2 Institute of Molecular Science and Technologies of the National Research Council (CNR-ISTM), SmartMatLab Centre, via Golgi 19, 20133 Milano, Italy
3 Department of Chemistry, University of Milano, INSTM RU, via Golgi 19, 20133 Milano, Italy
* Correspondence: serena.berardi@unife.it (S.B.); francesca.tessore@unimi.it (F.T.)

Received: 11 June 2019; Accepted: 3 July 2019; Published: 6 July 2019

Abstract: Two different high potential Zn(II) porphyrin designs carrying either 4 or 5 *meso* pentafluorophenyl moieties as electron acceptor groups and a further electron withdrawing branch inserted in either the β (**1**) or *meso* (**2**) position were tested in photoelectrosynthetic cells for HBr splitting. Photoaction spectra in the presence of HBr showed that red photons up to 700 nm could be harvested and converted and that **2** performed better than **1**, thanks to better electronic properties of the excited state, favored by the insertion of the benzothiadiazole electron withdrawing group. Photoanodic performances in the presence of HBr, however, remained low, due to inefficient regeneration of the oxidized sensitizer as a result of an insufficient driving force for Br^- oxidation.

Keywords: porphyrins; SnO_2; HBr splitting; sensitization

1. Introduction

In view of replacing traditional fossil fuels and reducing the resulting emissions of carbon dioxide, several strategies based on solar energy conversion and storage have been pursued [1,2]. In particular, along with the widespread photoinduced water splitting reaction [3,4], the splitting of hydrohalic acids (HX) in photoelectrosynthetic cell (PEC) set-ups has grown in interest among the scientific community [5–7]. Among the possible reactions, HBr splitting is the most promising [8,9], since the oxidation reaction yields Br_2, a liquid product easy to transport for its further use in fuel cells [10].

Photoanodes for bromide oxidation include TiO_2 or SnO_2/TiO_2 core-shell nanostructures functionalized with ruthenium polypyridyl based photosensitizers [11], as well as WO_3, SnO_2, and Sb-doped SnO_2 decorated with aggregated dyes belonging to the family of perylene diimides, reaching up to 1 mA/cm^2 photocurrent [9].

Being the primary light-harvesting pigments in photosynthesis, porphyrins have great potential in view of developing devices for solar energy conversion, due to their strong visible absorbance and synthetic tunability. Indeed, porphyrins display two sets of visible transitions, namely: (i) the Soret band, due to the excitation to the S_2 excited state, usually located at approximately 400 nm and characterized by high extinction coefficients ($\varepsilon = 10^5$ M^{-1} cm^{-1}); and (ii) broader and less intense ($\varepsilon = 10^3$–10^4 M^{-1} cm^{-1}) Q-bands at longer wavelengths (500–600 nm), due to excitations to the first singlet excited state (S_1). Furthermore, the photophysical and electrochemical properties of porphyrins can be tuned upon metalation or the introduction of tailored substituents [12–14], making them

excellent candidates for dye-sensitized regenerative solar cells [15,16], as well as for water splitting (when combined with suitable catalysts) [17,18].

In this work, we investigate the use of perfluorinated Zn(II) porphyrins in photoelectrosynthetic set-ups for HBr splitting, with the exploitation of two novel species (namely porphyrin **1** and **2** in Figure 1), with structural features aimed at optimizing the charge separation in the resulting dye-sensitized photoanode. In particular, while maintaining the functionalization of the *meso*-position with perfluorophenyl groups, known to increase the oxidation potential of the resulting dyes [18], we have introduced conjugated electron withdrawing linkers, terminating in cyanoacrylic groups for the anchoring to the semiconductor surface. Either β (in the case of **1**) or *meso* (in the case of **2**) positions have been functionalized in order to evaluate their impact on the sensitization efficiency in terms of directionality of the charge injection from the excited state. In addition, porphyrin **1** displays also an additional acceptor unit, namely the benzothiadiazole (BTD), which also contributes to the absorption of longer wavelengths. In this contribution we have explored the electronic and spectroscopic properties of such species applied to the sensitization of n-type SnO_2 substrates.

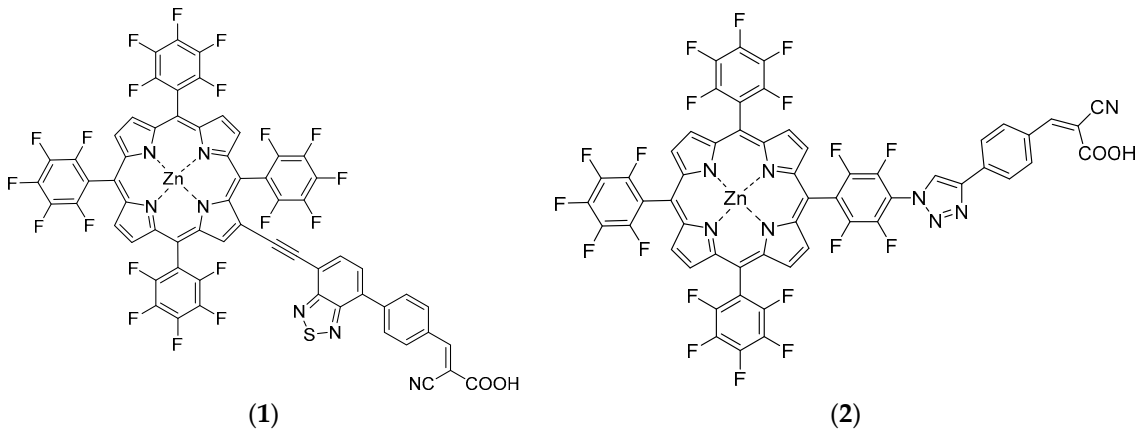

Figure 1. Zn^{II} porphyrins investigated in this work.

2. Experimental

2.1. Materials

All of the reagents and solvents were purchased from Sigma-Aldrich and used as received, except NEt_3 (freshly distilled over KOH) and CH_2Cl_2 used for the synthesis of H_2TPPF_{20} (distilled over CaH_2 immediately before use). Glassware was flame-dried under vacuum before use when necessary. Microwave assisted reactions were performed using a Milestone MicroSYNTH instrument. Silica gel for gravimetric chromatography (Geduran Si 60, 63–200 μm) and for flash chromatography (Kieselgel 60, 0.040–0.063 mm) were purchased from Merck. ^{1}H NMR and ^{19}F spectra were recorded on a Bruker AMX 300 and on a Bruker Avance DRX-400 in $CDCl_3$, or in THF–d_8 (Cambridge Isotope Laboratories, Inc., Tewksbury, MA, USA). Mass spectra were obtained with a Bruker-Daltonics ICR-FTMS APEX II with an electrospray ionization source or on a VG Autospec M246 magnetic mass spectrometer with a LSIMS ionic source.

2.2. Syntheses

2.2.1. H_2TPPF_{20}

A solution of 12.7 mmol of Pentafluorobenzaldehyde (2.50 g, 1.58 mL) and 12.7 mmol of freshly distilled pyrrole (0.85 g, 0.88 mL) in dry CH_2Cl_2 (1.5 L) was left under N_2 flux and vigorous stirring at RT in dark. After a few minutes, 3.6 mmol of BF_3•OEt_2 (0.51 g, 0.45 mL) were added, and the mixture

was allowed to react at RT overnight. Then, 12.8 mmol of DDQ (2.90 g) in dry CH_2Cl_2 (100 mL) were added and the mixture was refluxed for 2 h under N_2.

After cooling at RT, the crude was quickly filtered on a silica plug and then further purified by gravimetric chromatography (*n*-hexane:CH_2Cl_2 = 8:2), affording after evaporation of the solvents H_2TPPF_{20} as a purple powder (1.91 g, 62% yield).

^{1}H-NMR (400 MHz, $CDCl_3$, 25 °C, TMS), δ ppm: 9.01 (8H, s), −2.81 (2H, s).

^{19}F-NMR (400 MHz, $CDCl_3$, 25 °C), δ ppm: −136.42 (8F, dd), −151.20 (4F, t), −161.28 (8F, td).

2.2.2. $ZnTPPF_{20}$

A solution of 1.97 mmol of $Zn(CH_3CO_2)_2{\cdot}2H_2O$ (0.433 g, 4 eq.) in CH_3OH (30 mL) was added dropwise to a solution of 0.51 mmol of H_2TPPF_{20} (0.500 g) in $CHCl_3$ (80 mL), and the mixture was refluxed for 4 h, then cooled to RT, and the solvent was evaporated in vacuo. The resulting powder was dissolved in CH_2Cl_2 (50 mL) and washed with H_2O (3 × 20 mL). The organic phase was dried over Na_2SO_4, affording after evaporation of the solvent $ZnTPPF_{20}$ as a purple powder in almost quantitative yield.

^{1}H-NMR (400 MHz, $CDCl_3$, 25 °C, TMS), δ ppm: 9.03 (8H, s).

2.2.3. $ZnTPPF_{20}$-Br

In a two-neck round-bottom flask 0.089 mmol of $ZnTPPF_{20}$ (92.4 mg) were dissolved in CH_2Cl_2 (100 mL). After addition of 0.22 mmol of pyridine (17.6 mg), the mixture was heated to reflux, then 0.098 mmol of N-Bromosuccinimide (17.4 mg, 1.1 eq.) were added and the resulting mixture was left under reflux and vigorous stirring overnight.

The crude obtained after evaporation of the solvent was quickly checked by ^{1}H- and ^{19}F-NMR and used without further purification for the subsequent coupling reaction.

^{1}H-NMR (400 MHz, $CDCl_3$, 25 °C), δ ppm: 9.12 (1H, m), 9.00 (6H, m).

^{19}F-NMR (400 MHz, $CDCl_3$, 25 °C), δ, ppm: −137.03 (8F, m), −152.49 (4F, m), −162.11 (8F, m).

2.2.4. $ZnTPPF_{20}$-Si

In a microwave quartz vessel equipped with a magnetic stirrer, 0.127 mmol (142.3 mg) of $ZnTPPF_{20}$-Br and 0.0254 mmol (29.3 mg, 0.2 eq.) of $(Pd(PPh_3)_4)$ were dissolved in triethylamine (12 mL), under N_2 bubbling. Then, 0.637 mmol (196.6 mg, 5 eq.) of trihexylsilylacetylene and DMF (4 mL) were added to the solution. After 15 min of N_2 bubbling, 0.0254 mmol (4.8 mg, 0.2 eq.) of CuI were added. The vessel was placed into the microwave cavity and left under stirring at 120 °C for 1 h. After evaporation of the solvent in vacuo, the crude was purified by gravimetric chromatography (*n*-hexane: CH_2Cl_2 = 1:1), affording 152.0 mg of $ZnTPPF_{20}$-Si (89% yield) as an oily product.

^{1}H-NMR (400 MHz, $CDCl_3$, 25 °C) δ, ppm: 9.17 (1H, s), 8.99 (6H, m), 1.39 (24H, m), 0.94 (9H, m), 0.68 (6H, m)

^{19}F-NMR (400 MHz, $CDCl_3$, 25 °C) δ, ppm: −136.34 (6F, m), −137.40 (2F, d), −152.03 (4F, m), −161.71 (6F, s), −162.75 (2F, s).

2.2.5. $ZnTPPF_{20}$-H

In a dry Schlenk tube under N_2 flow, 1M THF solution of TBAF (0.250 mL, 2 eq.) was added dropwise under stirring to a solution of 0.111 (150 mg) of ZnF_{20}-Si in THF (5 mL). The mixture was stirred for 1 h at RT, then the reaction was quenched with H_2O (10 mL). The crude product was washed with H_2O (3 × 10 mL) and retrieved with CH_2Cl_2 (3 × 15 mL). The organic phase was dried over Na_2SO_4 and the solvent was evaporated in vacuo, affording 116.9 mg of $ZnTPPF_{20}$-H (>98% yield) as a purple powder.

^{1}H-NMR (400 MHz, $CDCl_3$, 25 °C) δ, ppm: 9.17 (1H, s), 8.93 (6H, m), 3.65 (1H, s)

^{19}F-NMR (400 MHz, $CDCl_3$, 25 °C) δ, ppm: −136.85 (8F, m), −151.99 (3F, m), −154.03 (1F, s), −161.92 (6F, s), −163.77 (2F, s).

2.2.6. $ZnTPPF_{20}$-BTD-CHO

In a dry Schlenk tube under N_2 flow, 0.0162 mmol (19 mg, 0.15 eq.) of ($Pd(PPh_3)_4$) were added to a solution of 0.108 mmol (115 mg) of $ZnTPPF_{20}$-H in triethylamine (3.5 mL). Under stirring, 0.217 mmol (69 mg, 2 eq.) of 4-(7-bromobenzo [1,2,5]thiadiazol-4-yl)benzaldehyde, THF (3.5 mL) and 0.0161 mmol (3 mg, 0.15 eq.) of CuI were added. Then, the mixture was kept under vigorous stirring and N2 atmosphere at reflux for 24 h. After removal of the solvents in vacuo, the crude substance was purified by gravimetric chromatography (*n*-hexane:CH_2Cl_2=1:1), collecting 40.0 mg of $ZnTPPF_{20}$-BTD-CHO as a purple-greenish powder (28% yield).

^{1}H-NMR (400 MHz, $CDCl_3$, 25 °C) δ, ppm: 10.16 (1H, s), 9.20 (1H, s), 8.84 (6H, m), 8.28 (2H, d), 8.14 (2H, d), 8.00 (1H, d), 7.97 (1H, d).

^{19}F-NMR (400 MHz, $CDCl_3$, 25 °C) δ, ppm: −136.81 (8F, broad s), −152.70 (3F, m), −153.84 (1F, m), −162.24 (6F, broad s), −163.20 (2F, s).

2.2.7. Porphyrin 1

In a dry Schlenk tube under N_2 flow, a solution of 0.155 mmol of cyanoacetic acid (13.0 mg, 5 eq.) in CH_3CN (0.75 mL) was added to 0.031 mmol (40.0 mg) of $ZnTPPF_{20}$-BTD-CHO in $CHCl_3$ (1.5 mL). After addition of piperidine (0.02 mL), the mixture was refluxed overnight under vigorous stirring. After removal of the solvents in vacuo, the residue was washed with a 2M aqueous solution of H_3PO_4 (5 mL) and extracted with CH_2Cl_2 (30 mL). The organic layer was dried over Na_2SO_4, the solvent was evaporated in vacuo, and the crude substance was purified by gravimetric chromatography (CH_2Cl_2:CH_3OH = 98:2), affording 20.7 mg of porphyrin **1** (49% yield) as a purple-greenish powder.

^{1}H-NMR (400 MHz, THF-d_8, 25 °C) δ, ppm: 9.54 (1H, s), 9.11 (6H, m), 8.39 (2H, d), 8.26 (2H, d), 8.18 (1H, d), 8.09 (1H, d).

^{19}F-NMR (400 MHz, THF-d_8, 25 °C) δ, ppm: −139.48 (2F, dd), −139.65 (6F, m), −155.89 (4F, t), −164.65 (8F, dd).

ESI-ITMS: *m/z* calculated for $C_{62}H_{15}F_{20}N_7O_2SZn$ = 1367.30; found = 1366.72 $[M-1]^-$.

2.2.8. H_2TPPF_{19}-N_3

In a dry Schlenk tube, 0.205 mmol (200 mg) of H_2TPPF_{20} and 0.205 mmol (13.4 mg) of NaN_3 were dissolved under N_2 flow in DMF (5 mL) and degassed through 3 freeze-pump-thaw cycles at −78 °C. The solution was stirred at reflux overnight. After evaporation of the solvent in vacuo, the residue was washed with H_2O (3 × 50 mL) and extracted with CH_2Cl_2 (3 × 20 mL). The organic phase was dried over Na_2SO_4. After evaporation of the solvent in vacuo, the crude residue was purified through gravimetric chromatography (*n*-hexane:CH_2Cl_2 = 8:2), affording 95.8 mg of H_2TPPF_{19}-N_3 (47% yield) as a purple powder.

^{1}H-NMR (400 MHz, $CDCl_3$, 25 °C) δ, ppm: 8.98 (8H, s), −2.89 (2H, s)

^{19}F-NMR (400 MHz, $CDCl_3$, 25 °C) δ, ppm: −136.42 (6F, dd), −137.7 (2F, m), −151.18 (1F, t), −151.49 (1F, dd), −161.26 (8F, td).

2.2.9. $ZnTPPF_{19}$-N_3

The metalation of H_2TPPF_{19}-N_3 was accomplished as described in Section 2.2.2.

^{1}H-NMR (400 MHz, $CDCl_3$, 25 °C) δ, ppm: 9.07 (8H, s).

^{19}F-NMR (400 MHz, $CDCl_3$, 25 °C) δ, ppm: −136.73 (6F, dd), −137.33 (2F, dd), −151.84 (1F, m), −151.49 (1F, dd), −161.68 (8F, m).

2.2.10. ZnTPPF19-click-CHO

In a dry Schlenk tube, 0.0960 mmol (101.9 mg) of $ZnTPPF_{19}$-N_3 and 0.115 mmol (14.9 mg, 1.2 eq.) of 4-ethynylbenzaldehyde were dissolved in a THF:CH_3CN = 1:1 mixture (7 mL), under N_2 flow. The solution was degassed through 3 cycles of freeze-pump-thaw at −78 °C, then 0.096 mmol (17 μL)

of N,N-diisopropilethylenammine and 0.0096 mmol (2 mg, 0.1 eq.) of CuI were added and the mixture was kept under stirring overnight at RT. The solvents were evaporated in vacuo and the crude residue was purified by gravimetric chromatography (CH_2Cl_2:n-hexane = 7:3, to remove the impurities; CH_2Cl_2:CH_3OH = 97:3, to recover the desired product), affording 68.2 mg of $ZnTPPF_{19}$-click-CHO (60% yield) as a purple powder.

^{1}H-NMR (400 MHz, $CDCl_3$, 25 °C) δ, ppm: 9.74 (1H, s), 9.08 (8H, m), 8.48 (1H, s), 7.94 (2H, d), 7.76 (2H, d).

^{19}F-NMR (400 MHz, $CDCl_3$, 25 °C) δ, ppm: −134.40 (2F, dd), −136.82 (6F, t), −146.57 (2F, m), −151.83 (3F, td), −161.67 (6F, td).

2.2.11. Porphyrin 2

In a dry Schlenk tube under N_2 flow, 0.0632 mmol (67.1 mg) of $ZnTPPF_{19}$-click-CHO were dissolved in $CHCl_3$ (5 mL), then 0.316 mmol (5 eq.) of cyanoacetic acid and piperidine (0.02 mL) were added under stirring. The mixture was refluxed overnight, then the solvent was evaporated in vacuo and the crude residue was washed with a saturated aqueous solution of NaCl (20 mL) and extracted with CH_2Cl_2 (3 × 10 mL). The organic phase was dried over Na_2SO_4, and the solvent was removed in vacuo. The crude residue was purified by gravimetric chromatography (CH_2Cl_2:CH_3OH = 9:1), affording 64.0 mg of porphyrin 2 (80% yield) as a purple powder.

^{1}H-NMR (400 MHz, THF-d_8, 25 °C) δ, ppm: 9.23 (2H, d), 9.18 (1H, s), 9.11 (5H, m), 8.55 (1H, broad s), 8.32 (4H, broad s).

^{19}F-NMR (400 MHz, THF-d_8, 25 °C) δ, ppm: −138.18 (2F, dd), −139.48 (6F, dd), −149.38 (2F, d), −156.15 (3F, dd), −165.12 (6F, td).

ESI-ITMS: *m*/*z* calculated for $C_{56}H_{15}F_{19}N_8O_2Zn$ = 1258.17; found = 1255.82 $[M-1]^-$.

Photoanode Preparation

Colloidal SnO_2 paste was prepared by following a literature procedure [19]. Fluorine tin oxide glass (FTO TEC 8, Pilkington, St Helens, UK) cleaning was performed by sonicating the slides in an Alconox® solution for 10 min and in 2-propanol for a further 10 min. After blow-drying the resulting FTOs, a thin blocking/adhesion layer of SnO_2 was obtained by spin coating a 0.3 M $SnCl_2$ solution in ethanol, followed by heating at 500 °C for 15 min in air. After cooling these substrates at room temperature, the SnO_2 paste was blade cast onto them to obtain a wet film, which was fired at 500 °C for 30 min, leading to a mesoporous network composed of SnO_2.[9] Finally, an overlayer of TiO_2, serving both as a passivation layer and to improve dye adsorption, was formed by immersion of the SnO_2 films in an aqueous 0.4 M Titanium tetrachloride ($TiCl_4$) solution for 12 h, followed by rinsing with DI water and heating at 450 °C for 30 min. Staining of the resulting photoanodes was carried out by immersion in a 2 μM solution of each porphyrin in a toluene/ethanol 1:1 mixture containing 2×10^{-5} M chenodeoxycholic acid as an anti-aggregating agent. Preferred adsorption times were 6 h for **1** and 14 h for **2**.

Spectroscopic and Electrochemical Measurements in Solution

Electronic absorption spectra of porphyrins **1** and **2** in solution were recorded at room temperature in toluene, using a Shimadzu UV3600 spectrophotometer and quartz cuvettes with 1 cm optical path length. Photoluminescence experiments were carried out at room temperature, and photoluminescence quantum yields were measured with a C11347 Quantaurus–QY Absolute Photoluminescence Quantum Yield Spectrometer (Hamamatsu Photonics K.K., Shizuoka, Japan), equipped with a 150 W Xenon lamp, an integrating sphere, and a multi-channel detector. Steady state emission and excitation spectra and photoluminescence lifetimes were obtained with a FLS 980 spectrofluorimeter (Edinburgh Instrument Ltd., Livingston, UK). Continuous excitation for the steady state measurements was provided by a 450 W Xenon arc lamp. Photoluminescence lifetime measurements were performed using an Edinburgh Picosecond Pulsed Diode Laser EPL-445 (Edinburgh Instruments Ltd.), with central

wavelength of 442.2 nm and repetition rate of 20 MHz, by Time-Correlated Single-Photon Counting method (TCSPC).

The voltammetric studies of porphyrins in solution were performed in a 4 cm^3 cell, with 5×10^{-4} M solutions in DMF (Aldrich, 99.8%) with 0.1 M tetrabutylammonium perchlorate ($TBAClO_4$, Fluka) as the supporting electrolyte. The solutions were de-aerated by N_2 bubbling. The ohmic drop was compensated by the positive feedback technique. The experiments were carried out using an AUTOLAB PGSTAT potentiostat (EcoChemie, Utrecht, The Netherlands) run by a PC with GPES software. Cyclic voltammetry (CV) investigations were carried out at scan rates typically ranging 0.05 to 2 V s^{-1}; differential pulse voltammetry (DPV) curves (step potential: 5 mV; modulation amplitude: 50 mV) were also recorded for each compound as both oxidative and reductive scans. The working electrode was a glassy carbon one (AMEL, diameter = 1.5 mm) cleaned by synthetic diamond powder (Aldrich, diameter = 1 μm) on a wet cloth (STRUERS DP-NAP); the counter electrode was a platinum disk or wire. The operating reference electrode was an aqueous saturated calomel electrode, but the potentials were ultimately referred to the Fc^+/Fc (ferrocinium/ferrocene) couple (the intersolvental redox potential reference currently recommended by IUPAC by both external and internal standardization [20,21]. To prevent water and chloride leakage into the working solution, a compartment filled with the operating medium and ending with a porous frit was interposed between the reference electrode and the cell.

Photoelectrochemical Measurements

Photoelectrochemical measurements were carried out on a PGSTAT 302N potentiostat in a three-electrode configuration, using SCE and Pt wire, respectively, as the reference and the counter electrode. A LOT-Oriel solar simulator, equipped with an AM 1.5 G filter, was used as the illumination source, and set to 0.1 W cm^{-2} incident irradiance power by means of a Power Meter (Newport 1918-C). Current-voltage curves, recorded at 10 mV/s, were repeated by cycling the photoanodes until an overlapping response upon subsequent scans (stationary state) was achieved. Current–voltage curves under shuttered illumination were acquired by manually chopping the excitation source. Incident photon-to-current conversion efficiency (IPCE) was measured in a three-electrode configuration under the monochromatic illumination generated by an air-cooled Luxtel 175 W Xe lamp coupled to an Applied Photophysics monochromator. The resulting photocurrent, recorded at the constant potential of 0.7 V versus SCE, was measured by a PGSTAT 302N potentiostat. Unless otherwise stated, all the potential values are given versus the standard calomel electrode, SCE.

Transient Absorption Spectroscopy

Transient absorption spectroscopy (TAS) was performed with a previously described apparatus [22], using the 532 nm harmonic of a nanosecond Nd:YAG laser (Continuum Surelite II) and a monochromatic probe beam. Transient measurements on thin films were obtained by orienting the electrodes at an angle of approximately 45° with respect to the excitation, with a laser fluence of 3.3 mJ/cm^2/pulse, and without pulsing the probe beam. The probe light which was transmitted by the sample was passed through a stack of two 532 nm notch filters to eliminate the scattered laser and focused into a second group of 150 lines/mm grating before reaching the photomultiplier biased at 470 V. Spectra on the ms/sub ms timescale were recorded with an oscilloscope input impedance of 1 MΩ to pre-amplify the differential absorbance (ΔA) traces, which were averaged over 100 shots to obtain a good Signal-to-Noise (S/N) ratio. Transient kinetics under electrochemical polarization were recorded with an EcoChemie PGSTAT302/N potentiostat, employing a platinum electrode as a counter electrode in a two-electrode configuration. The decay traces were fitted with a biexponential function in order to obtain a smooth curve to extract the half-life ($\tau_{1/2}$) of the process. The normalized kinetic decays at 0.7 V versus Pt were used for the calculation of the regeneration constant (k_{reg}), in the presence of the Br^- electrolyte (NaBr 0.3M, HBr 0.1M), from the recombination constant (k_{rec}),

computed from $\tau_{1/2}$ of the charge separated state in the blank electrolyte ($HClO_4$) ($k_{rec} = 1/\tau_{1/2,blank}$), according to the equations:

$$k_{reg} = k_{Br-} - k_{rec} \quad (1)$$

$$k_{Br-} = 1/\tau_{1/2,Br-} \quad (2)$$

where $\tau_{1/2,Br-}$ is the half-life of the charge-separated state in the presence of Br^-.

From the regeneration constant, regeneration efficiency related to Br^- was estimated according to:

$$\eta_{reg} = k_{reg}/(k_{reg} + k_{rec}) \quad (3)$$

Computational Chemistry

All calculations were performed with Gaussian 09 [23]. Ground state structures of **1** and **2** were optimized at the B3LYP/DGDZVP level [24] in vacuo. Singlet electronic transitions were computed on the optimized geometries at the TDDFT/B3LYP/6-311G d,p level in toluene treated as a dielectric continuum (IEFPCM). Orbital isosurfaces were plotted with Gaussview 5 and electron/hole density maps were obtained with Multiwfn 3.3.9 [25] at an isolevel of 0.001.

3. Results and Discussion

3.1. Syntheses

Porphyrin **1** was prepared as reported in Scheme 1.

The H_2TPPF_{20} core was prepared by the Lindsey method [26] in 62% yield, condensing pyrrole with pentafluorophenylbenzaldehyde in the presence of catalytic amounts of $BF_3(OEt)_2$, and then oxidizing the porphyrinogen with 2,3-dichloro-5,6-dicyano-1,4-benzoquinone.

The complexation of H_2TPPF_{20} with $Zn(CH_3CO_2)_2{\cdot}H_2O$ afforded $ZnTPPF_{20}$ in almost quantitative yield. Then, $ZnTPPF_{20}$ was monobrominated in β-pyrrolic position by reaction with N-bromosuccinimide (70% yield), affording $ZnTPPF_{20}$-Br, which was used for a Sonogashira's coupling with trihexylsilylacetylene, $[Pd(PPh_3)_4]$ and CuI, following the microwave-assisted approach (1 h, 120 °C) developed previously [27]. $ZnTPPF_{20}$-Si was obtained at 89% yield. After removal of the protective silyl group with tetrabutylammonium fluoride in THF, $ZnTPPF_{20}$-H was used for a second Sonogashira's coupling (24 h at 80 °C) with 4-(7-bromobenzo[1,2,5]thiadiazol-4-yl)benzaldehyde (previously prepared as reported in Scheme S1) in a triethylamine/THF mixture as the solvent and catalytic amounts of $[Pd(PPh_3)_4]$ and CuI, affording $ZnTPPF_{20}$-BTD-CHO (28% yield). The final step was a Knoevenagel condensation between $ZnTPPF_{20}$-BTD-CHO and cyanoacetic acid with piperidine as a base in a $CHCl_3/CH_3CN$ mixture, affording **1** 49% yield.

The synthesis of porphyrin **2** was accomplished as depicted in Scheme 2.

The selective nucleophilic substitution [28] of only one of the four *para* fluorine atoms of the pentafluorophenyl rings in the 5,10,15,20 *meso*-position of H_2TPPF_{20} core was achieved (47% yield) by reaction of the free base with 1 equivalent of sodium azide with N,N-dimethylformamide as a solvent, followed by complexation with Zn^{II} in almost quantitative yield. Then, a CuI-catalyzed Huisgen 1,3-dipolar cycloaddition [29] between $ZnTPPF_{19}$-N_3 and 4-ethynlbenzaldehyde in a THF/CH_3CN mixture with N,N-diisopropylethylamine as a base gave $ZnTPPF_{19}$-click-CHO (60% yield). As the final step, a Knoevenagel condensation between $ZnTPPF_{19}$-click-CHO and cyanoacetic acid with piperidine as a base in a $CHCl_3/CH_3CN$ mixture afforded porphyrin **2** at 80% yield.

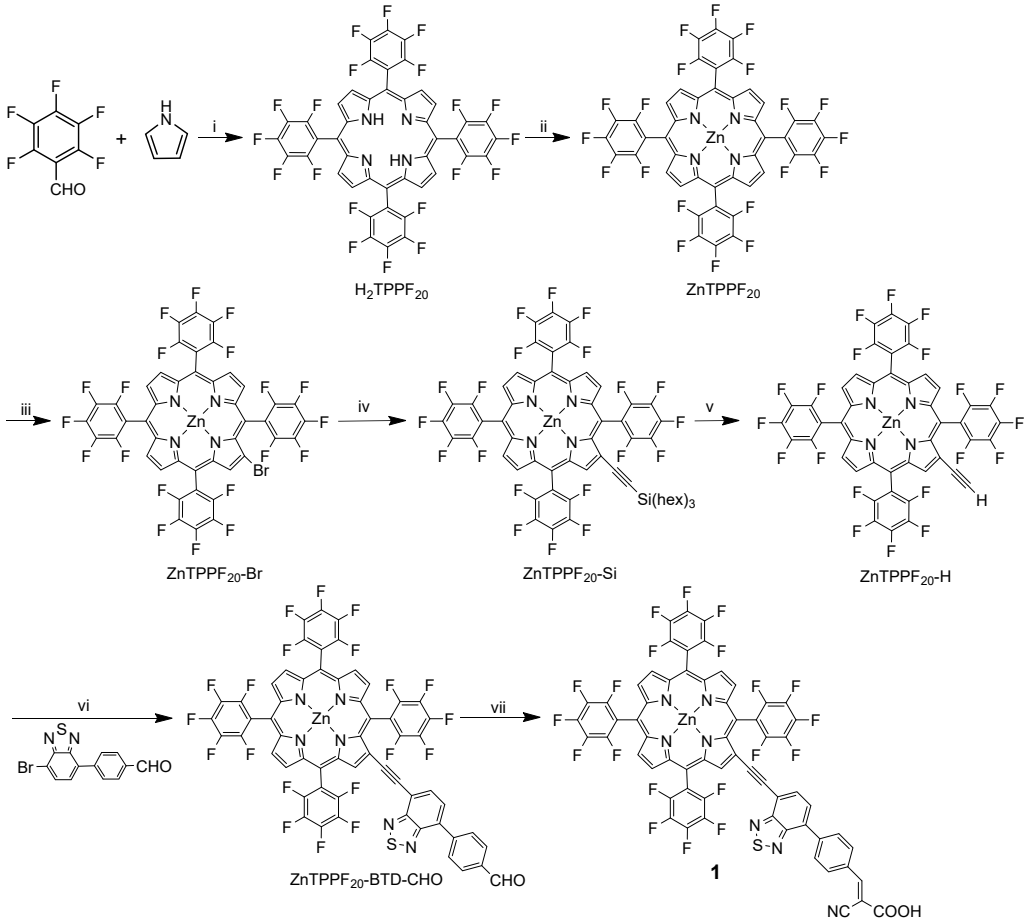

i) a) $BF_3(OEt_2)$, N_2, CH_2Cl_2, RT, overnight; b) DDQ, CH_2Cl_2, RT, 2hrs. ii) $Zn(CH_3CO_2)_2.2H_2O$, $CHCl_3$, CH_3OH, reflux, 4hrs . iii) NBS, pyridine, CH_2Cl_2, reflux, overnight.
iv) trihexylsilylacetylene, NEt_3, $[Pd(PPh_3)_4]$, CuI, DMF, MW 120°C, 1hr. v) TBAF, THF, N_2, RT, 1hr. vi) $[Pd(PPh_3)_4]$, CuI, NEt_3, THF, N_2, 80°C, 24hrs. vii) $CNCH_2COOH$, $CHCl_3$, CH_3CN, piperidine, N_2, reflux, overnight

Scheme 1. Synthesis of dye 1.

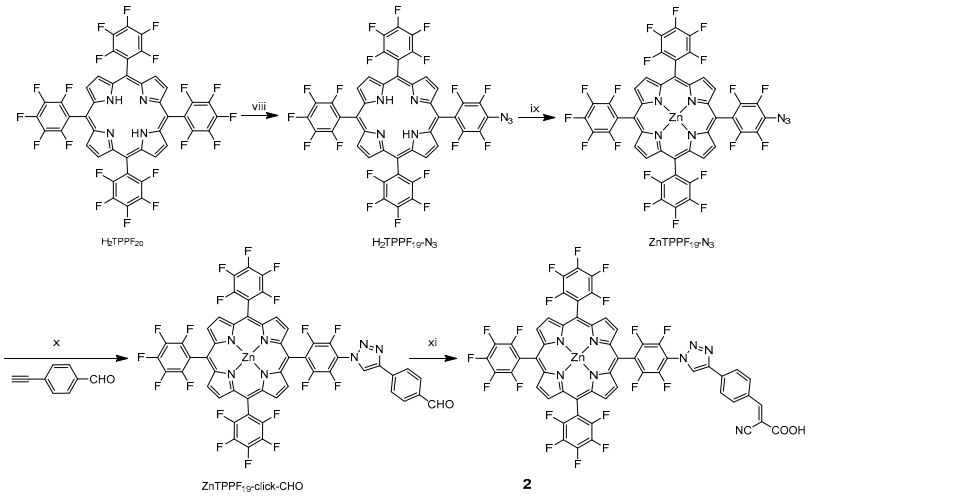

viii) NaN_3, N_2, DMF, 60°C, 3hrs. ix) $Zn(CH_3CO_2)_2.2H_2O$, $CHCl_3$, CH_3OH, reflux, 4hrs . x) DIPEA, CuI, N_2, THF/CH_3CN=1/1, RT, overnight. xi) $CNCH_2COOH$, $CHCl_3$, CH_3CN, piperidine, N_2, reflux, overnight

Scheme 2. Synthesis of dye 2.

The new dyes were characterized by ^{1}H and ^{19}F-NMR spectroscopy and by ESI-MS spectrometry (see Experimental section).

3.2. Spectroscopic and Electrochemical Properties in Solution

Porphyrins **1** and **2** were investigated by UV-vis absorption and emission spectroscopies in toluene solution. The ε-normalized spectra are reported in Figure 2, and the corresponding data in Table 1.

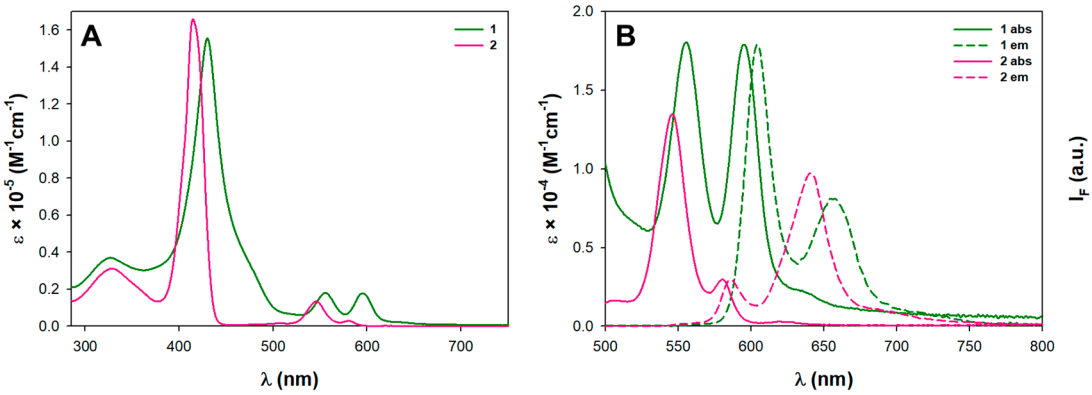

Figure 2. (**A**) Full UV-vis absorption spectra of **1** and **2** recorded in toluene solution; (**B**) spectra of the Q bands and normalized emission spectra recorded in toluene solution at 10^{-6} M concentration.

The UV-vis absorption spectrum of **1** (Figure 2A) shows the typical pattern of β-pyrrolic porphyrins, with a broadened Soret or B band (at 430 nm) and two well-defined Q bands (at 555 and 595 nm). The broadening of the B band is the result of the electronic and steric interaction between the porphyrin ring and the BTD moiety of the anchoring unit in the β-pyrrolic position, rather than an additional absorption peak due to the BTD unit itself [30]. Moreover, the spectrum is red-shifted in comparison to that of **2**, confirming for the β-substituted molecular architecture a more favorable conjugation and charge transfer between the porphyrin core and the anchoring unit, with increased light-harvesting [31].

The UV-vis absorption spectrum of **2** (Figure 2A) displays a sharp and intense B band (at 415 nm) and apparently only one Q band (at 546 nm), with a pattern more similar to that of a *meso*-substituted porphyrin [12]. However, a second Q band featuring a very low intensity can be detected at 580 nm (Figure 2B).

The emission spectra (Figure 2B) are a mirror copy of the absorption of the Q bands. Although, at first sight, **2** seems to be an exception, the absorption intensity of its Q band at higher energy is likely affected by the broadening of the B band. Minimal Stokes shifts between the peak of the absorption band at lower energy and the peak of the emission band at higher energy are observed, confirming the rigidity of these systems and reduced molecular distortions during the absorption and emission processes.

The comparison between the UV-vis absorption and emission spectra allowed us to assess the E^{0-0} value, which corresponds to the spectroscopic HOMO-LUMO energy gap (see Table 1). In agreement with the enhanced push-pull character imparted by the presence of the BTD unit, the HOMO-LUMO gap of **1** is lower than that of **2**.

The characterization of the excited states of **1** and **2** in solution was completed by the measurement of the lifetime by the single photon counting technique using a pulse laser source at 442 nm (see Experimental Section). From the convolution fit of the decay profiles (Figure S1), comparable τ values were in the range of 1.3–1.4 (Table 1).

Neverthless, the fluorescence quantum yield (QY, Φ) of **2** is more than twice that of **1** (Table 1).

Table 1. Absorption and emission data in toluene solution.

Dye	λ_B/nm (log ε)	λ_Q/nm (log ε)		λ_{ex}/nm	λ_{em}/nm		Φ/% [a]	τ/ns [a]	E^{0-0}/eV
1	**430 (5.19)**	555 (4.26)	595 (4.25)	431	604	654	5.6	1.40	2.07
2	415 (5.22)	546 (4.13)	580 (3.48)	419	586	640	2.4	1.30	2.13

[a] These values were recorded at 10^{-6} M concentration.

The energy levels of the oxidation and reduction processes and the chemical and electrochemical reversibility of **1** and **2** were evaluated by cyclic voltammetry (CV) experiments in order to state their implementation in a photoelectrochemical cell for efficient HBr splitting. The CV patterns are reported in Figures S2A and S3A, and their key features are summarized in Table S1.

For porphyrin **2** one oxidation peak and two reduction peaks are observed in the potential window investigated (Figure S3A), whereas for porphyrin **1** a third reduction peak is evident due to the presence of the electron-rich BTD unit (Figure S2A). In particular, the clear presence of only one oxidation peak reflects the electron-poor features of this class of perfluorinated porphyrins, where oxidation processes are less accessible. The oxidation peak and the first reduction peak of both dyes are reversible or quasi-reversible from both the electrochemical and chemical point of view, allowing the calculation of formal potentials $E^{0'}{}_{Ia}$ and $E^{0'}{}_{Ic}$ for the first oxidation (anodic) and first reduction (cathodic) processes, respectively, in the operating solvent (formal potentials $E^{0'}$ approximate standard potentials E^0 under the assumption of neglecting activity coefficients).

The experimental $E^{0'}$ values allowed evaluation of the electrochemical HOMO and LUMO energy levels [12] and the electrochemical HOMO–LUMO energy gaps E_g (Table S1), which are in good agreement with the spectroscopic E^{0-0} (Table 1), confirming the same trend.

Differential pulse voltammetry (DPV) experiments allowed better-defined forward and backward waves of the oxidation and reduction processes to be obtained (Figures S2B and S3B), allowed determination of the value of the peak potentials $E_{p,Ia}$ and $E_{p,Ic}$, and calculation of $E^{0'}{}_{Ia}$ and $E^{0'}{}_{Ic}$ by Equations (4) and (5) (where ΔE is the modulation amplitude):

$$E^{0'}{}_{Ia} = E_{p,Ia} + \Delta E/2 \quad (4)$$

$$E^{0'}{}_{Ic} = E_{p,Ic} - \Delta E/2 \quad (5)$$

The HOMO and LUMO energy levels and the HOMO–LUMO energy gaps (E_g) derived from DPV measurements are summarized in Table 2.

Table 2. Electrochemical properties of porphyrins **1** and **2**, and electrochemical HOMO and LUMO energy levels derived from $E^{0'}{}_{Ia}$ and $E^{0'}{}_{Ic}$ (or $E_{p,Ia}$ and $E_{p,Ic}$), all referred to the ferrocenium/ferrocene redox couple.

Dye	$E_{p,Ia}$/V (Fc^+|Fc)	$E^{0'}{}_{Ia}$/V (Fc^+|Fc)	$E_{p,Ic}$/V (Fc^+|Fc)	$E^{0'}{}_{Ic}$/V (Fc^+|Fc)	HOMO/eV	LUMO/eV	$\Delta E^{0'}$/V ($E_{g,EC}$/eV)
1	0.80	0.86	−1.29	−1.32	−5.63	−3.48	2.15
2	0.75	0.77	−1.43	−1.46	−5.58	−3.34	2.24

DPV data are in perfect correspondence with those obtained by CV (Table S1).

The electrochemical measurements confirm a more conjugated character for the β-substituted porphyrin **1**, having a narrower HOMO-LUMO gap.

The slight difference between the spectroscopic (Table 1) and the electrochemical (Table 2) energy gaps is due to some issues related to the LUMO energy level. Indeed, while for a neutral molecule the LUMO corresponds to a light-promoted transition, in an electrochemical process it is the addition of an electron to the neutral molecule, generating a radical anion species. Therefore, to better assess the HOMO and LUMO energy levels of **1** and **2**, to match with the energy levels of the components of the photoelectrochemical cell, we calculated the LUMO by Equation (6):

$$E_{LUMO} = E^{0-0} - E_{HOMO} \quad (6)$$

where E^{0-0} is the spectroscopic energy gap (Table 1) and E_{HOMO} is the value obtained by the electrochemical measurements for the first oxidation process (Table 1).

For **1** and **2** the calculated LUMO levels are −3.56 eV and −3.45 eV, respectively.

As depicted in Figure 3, the energetics of dyes **1** and **2** in solution are suitable to envisage their application in a photoelectrochemical cell for HBr splitting. Indeed, they have an electrochemical LUMO at higher energy than that of TiO_2 and SnO_2 conduction band, offering the exoergonic photoinjection of electrons from the excited states of the dyes into the semiconductor.

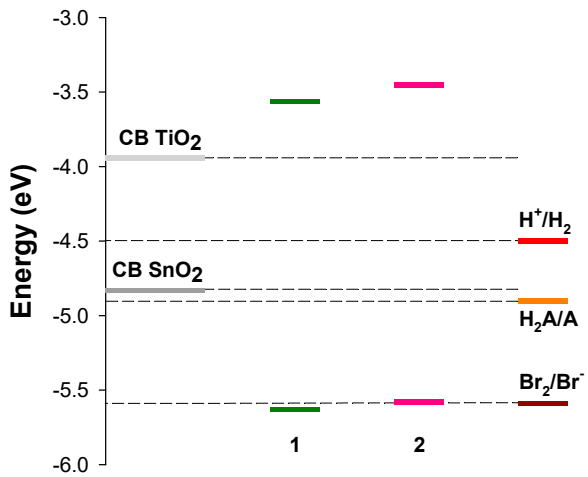

Figure 3. HOMO–LUMO levels for porphyrins **1** and **2.**

In particular, the introduction of a BTD moiety in β-pyrrolic position induces a sizable stabilization of the LUMO level, in accordance with the increased electron-withdrawing ability of the acceptor unit [30].

Considering the Br_2/Br^- redox couple, both HOMO dyes are nearly isoergonic with the Br_2/Br^- couple. Further, **1**, displaying a HOMO energy lower than that of the redox couple, should have a slight advantage for better regeneration compared to **2**.

3.3. Computational Results

Ground state optimized structures of Zn(II) porphyrinates 1 and 2 are shown in Figure 4, along with with the orbitals involved in the main visible transitions, reported in Figure 5 together with the Electron Density Difference Maps (EDDMs) associated to the main optical transitions originating in the Q and B bands. The Zn(II) porphyrinates have a planar tetrapyrroling ring whith pentafluorophenyl groups oriented at right angles with respect to the ring plane. In the β-substituted moiety 2, the BTD group form a dihedral angle of 36.5° with respect to the macrocyclic ring. The benzene ring bridging BTD with the cyano acrylic group displays a tilt of 34.5° with respect to the former. In principle, these angles are the consequence of a certain degree of electronic delocalization between the porphyrin core and the acceptor arm, tasked with binding the metal oxide and providing coupling between the excited state and the conduction band of SnO_2. This is confirmed by the spatial distribution of the frontier orbitals, which, consistent with the strong electron acceptor character of BTD, show extended delocalization of the HOMO-2, HOMO, LUMO, and LUMO+2. By contrast in porphyrin 2, the fluorinated phenyl ring bearing the triazole bridge is oriented at 90 degrees with respect to the plane, interrupting electronic conjugation. As a consequence, the frontier orbitals of 2 show two pairs of nearly degenerate orbitals all centred on the porphyrin core, a situation recalling the classical "Gouterman 4 orbital model" [32] typical of symmetric *D4h* porphyrins. No electronic distribution on the cyano-acrylic group is present at the level of HOMO-1, HOMO, LUMO, and LUMO+1, whereas HOMO-2 and LUMO+2 are entirely localized on the planar arm constituted by the triazole connected to the cyanoacrylic group via a phenyl spacer.

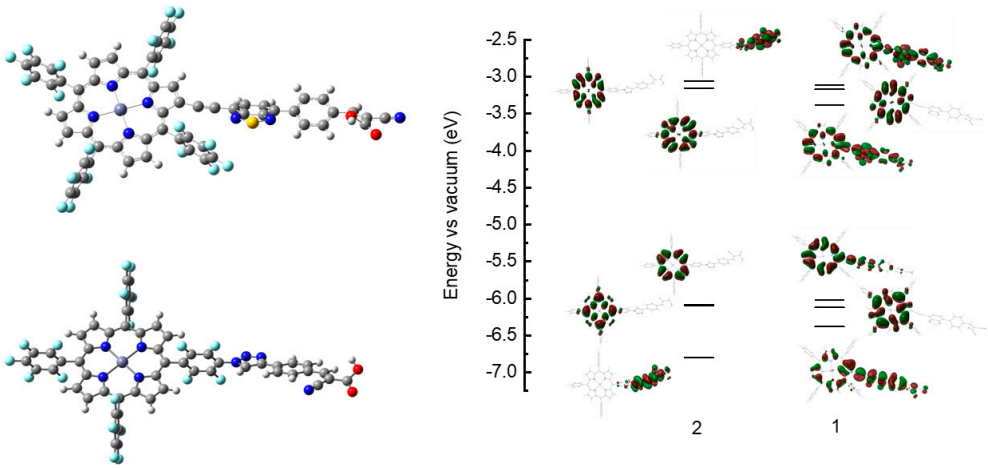

Figure 4. Left: optimized ground state geometries of the meso-porphyrin 1 and the β-substituted porphyrin 2. **Right**: frontier energy levels associated to their respective Kohn-Sham Orbitals (KSO) (B3LYP-6311G d,p).

TDDFT usually describes the electronic transitions with a mixing of single KSO contributions, therefore the spatial redistribution of the electronic density following optical excitation is conveniently described by EDDMs, showing the transitions in term of holes (decreased electronic density) and electrons. First, we observe that in both cases, despite the difficulty of TDDFT to describe long range charge transfer states (CT), the computation reproduces two distinct regions with stronger (B bands) and weaker oscillator strengths (Q bands). The energy of the computed transitions is generally higher with respect to the experimental bands, but the errors are not large, varying between 0.22 (1) and 0.13 eV (2). Correction by these systematic amounts results in a reasonable match of the computed vertical transitions with the experimentally observed bands (Figure 5).

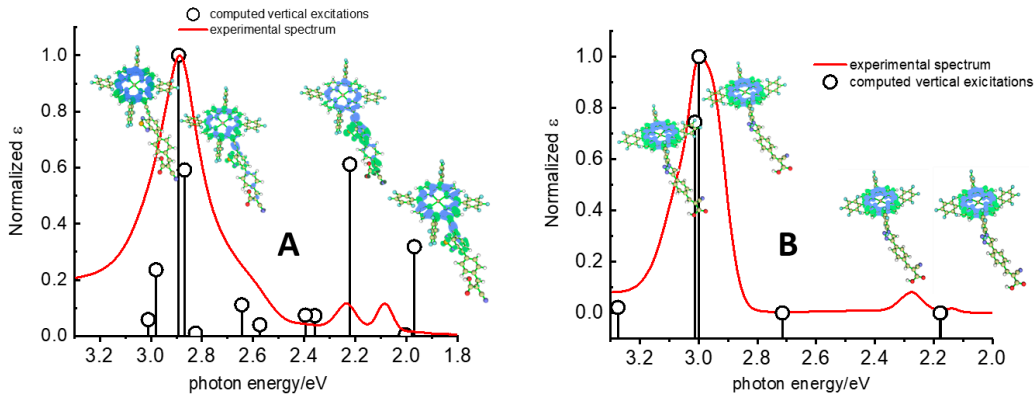

Figure 5. Computed vertical transitions at the TDDFT 6311 Gd,p level (black vertical bars) overlapped with the experimental spectrum. Vertical transitions were red shifted by 0.22 eV (**A**; **1**) and 0.13 eV (**B**; **2**) to match the Soret band maximum with the most intense vertical transition. EDDMs (isovalue 10^{-3}) associated with the most intense transitions in Q and B band region are shown as insets. Increased electron density is indicated by a green surface, depleted electron density (i.e., a "hole") is indicated by the blue surface.

EDDMs show essentially no involvement of the linker arm in the case of **2**, consistent with the localization of the frontier orbitals on the macrocycle. On the other hand, porphyrin **1** shows a larger electronic delocalization on the electron accepting arm, at least in the case of the most intense transitions between 2 and 2.2 eV, corresponding to the Q band region. However, the lowest singlet state has no electron density on the cyano-acrylic group, and electron delocalization does not extend beyond the

BTD acceptor. A larger electron density is seen in correspondence of the excitation at 2.22 eV, whereas the EDDMs associated with the Soret band do not show substantial involvement of the BTD linker but remain mainly confined within the tetrapyrrolic ring, probably due to the inductive effect caused by the perfluorinated rings.

The electron transfer rate constant from the excited dye to the semiconductor can be conveniently described within the framework of the semiclassical Marcus Model, according to [33]:

$$k_{et} = \frac{2\pi}{\hbar} H_{RP}^2 (4\pi\lambda kT)^{-1/2} \exp\left(-\frac{\left(\lambda + \Delta G^0\right)^2}{4\lambda kT}\right) \quad (7)$$

$$H_{RP} = \langle \psi_R | H | \psi_P \rangle \quad (8)$$

where H_{RP} is the electronic matrix element determined by the wavefunctions of the reactant and the product of the electron transfer reaction where the electron can reside either in the excited molecular sensitizer in the R = reactant state or in the semiconductor in the P = product state; ΔG^0 is the free energy for electron injection and λ is the reorganization energy associated with the electron transfer. In the most favorable thermodynamic case, where $\Delta G^0 = -\lambda$, the electron transfer rate will be controlled by the electronic coupling H_{RP}.

From the computational results, we can conclude that probably neither porphyrin has optimal electron/hole spatial distribution of the excited state to perform efficient injection into the n-type semiconductor, since, as a result of the excitation, the shift of electron density on the linker arm, which connects the sensitizer to the semiconductor surface, is comparatively small with respect to that remaining on the porphyrin ring, which is relatively remote from the SnO_2 surface. With this limitation present, the calculations also suggest that photoinduced charge injection by **1** should be more efficient than in the case of **2**, since, when population of the lowest singlet states is achieved, an excess of electron density is created on the BTD pendant in relative proximity to the semiconductor surface. The n-type sensitization capability of these dyes will be, thus, experimentally assessed in the forthcoming section.

3.4. Spectroscopic and Photoelectrochemical Characterization of the Sensitized Photoanodes

SnO_2 photoanodes, treated with $TiCl_4$, have been sensitized by soaking in a 0.1 mM dye solution. It is worth noting that the conduction band edge of SnO_2 should allow for a large driving force for electron injection from the excited states of the two dyes. Indeed, SnO_2, or SnO_2/TiO_2 core-shell nanostructures, have been used as semiconductive scaffolds in dye-sensitized devices for solar energy conversion, particularly when the excited states of some sensitizers were too poorly reduced to allow for an ultrafast injection into TiO_2 [34–36]. At the same time, the hydrophilic properties of TiO_2 may enhance the higher uptake of the porphyrinic dyes via formation of ester-like bonds between COOH in the linker and OH groups at the metal oxide surface, resulting in better coverage and light harvesting. For the sake of notation simplicity, we will refer to the $TiCl_4$-treated SnO_2 photoanodes dyed with the respective porphyrins as SnO_2-**1** and SnO_2-**2**, as this is the only type of semiconductor substrate used in the present study.

The UV-vis spectra of SnO_2-**1** and SnO_2-**2** are reported in Figure 6, showing that light harvesting can be extended at $\lambda > 650$ nm with the β porphyrin **1**. Consistent with the absorption spectra recorded in solution and with the calculations, the presence of an increased charge transfer (CT) character broadens the B band, which bears the contribution of multiple electronic transitions (at least 6, according to Figure 5) and, thus, extends from 400 to 500 nm. Two distinct Q bands centered at 560 and 600 nm, respectively, cover the red part of the visible spectrum. Further, **1** achieves similar maximum maximum absorbance (approximately 0.7) but its main bands are narrower compared to **2**, as a result of nearly degenerate transitions localized on the tetrapyrrolic cycle, analogous to those of a symmetric porphyrin, showing a single Q band at 560 nm with two shoulders at 520 and 590 nm and the Soret band centered at 430 nm.

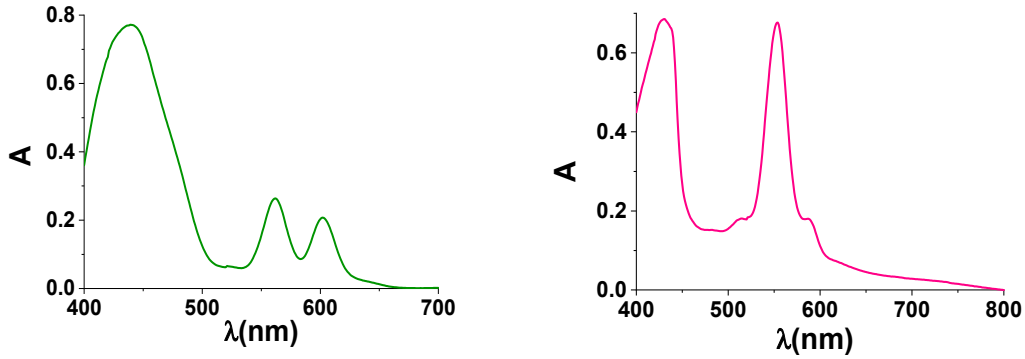

Figure 6. Electronic spectra of SnO_2-**1** (**left**) and SnO_2-**2** (**right**). Spectra were recorded in transmission mode against a blank SnO_2 photoanode for background correction.

The photoanodic performance was initially evaluated in the presence of the presence of 0.1 M ascorbic acid (AA; pH 5), which is easy to oxidize and performs as an efficient hole scavenger. Under such conditions, the regeneration efficiency (η_{reg}) of the oxidized sensitizer should be nearly quantitative and the photocurrent should, thus, be limited by the light harvesting efficiency (LHE = $1 - 10^{-A}$) and by the charge injection yield (Φ_{inj}).

Current/potential (J/E) characteristics registered under Air Mass (AM)1.5G (0.1 W/cm^2) in the presence of both continuous and shuttered illumination are reported in Figure 7. The photocurrent onset is observed at −0.15 V versus SCE and increases upon anodic polarization, consistent with the n-type properties of the semiconductor/liquid electrolyte junction (SCLEJ), up to 3 mA/cm^2 in the case of **1** at 0.6 V versus SCE. A well-defined photoanodic plateau is, however, not observed, as the dark current starts to rise at 0.4 V versus SCE, due to the electrochemical oxidation of AA, probably through pinholes in the mesoporous SnO_2 film. Photoanodic transients match reasonably well with the shape of the steady state curve and allow quantification of precisely the magnitude of the net photocurrent; approximately 2.85 mA/cm^2 with SnO_2-**1**, which is approximately 40% higher than that found for SnO_2-**2** at equivalent voltage, as a probable result of broader light harvesting and better injection from the former.

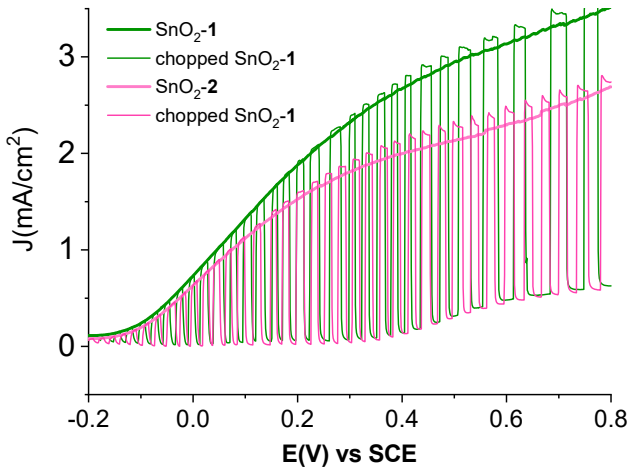

Figure 7. J/E curves in the presence of 0.1 M AA under AM 1.5G illumination. Illumination from the FTO side, potential sweep rate 10 mV/s.

The encouraging results obtained in the presence of the ascorbic acid as a scavenger prompted us to test the photoanodes for the photoinduced HBr splitting, which is the main target of our study. We decided to operate at pH 1 (0.1 M HBr) in order to avoid the formation of bromine oxo-anions. Figure 8 shows the J/E curves recorded for SnO_2-**1** and SnO_2-**2** photoanodes under AM 1.5 G (0.1 W/cm^2)

illumination. The position of the onset potential, estimated to be 0.05 V from the analysis of the chopped curves, is approximately 0.2 V more anodic than that obtained for ascorbic acid oxidation and can be ascribed to the Nernstian shift of the flat band voltage of SnO_2 (59 mV × ΔpH) due to the pH difference of AA compared to HBr. Nevertheless, compared to the electrochemical oxidation of Br^- at SnO_2 working electrodes, which is onset at approximately 0.8 V versus SCE, the photoactive interface is able to store approximately 0.6 V in the form of photovoltage. The limiting photocurrent, which corresponds to the maximum rate of photoxodiation of Br^- at the SCLEJ is already found starting from approximately 0.3 V versus SCE but values are approximately 10 times lower than in the AA case, reaching up 0.3 and 0.23 mA/cm^2 at 0.4 V, respectively, for SnO_2-**1** and SnO_2-**2**. Large overshootings in the activation region of the curves, between 0.1 and 0.25 V versus SCE (Figure 5), coupled to the observation that J/Es collected by illumination through the electron collector (i.e., from the FTO side) gave substantially better results than those acquired by electrolyte side excitation (see Figure S4 for a comparison), indicated a substantial amount of electronic recombination, probably due to inefficient regeneration of the photogenerated oxidized sensitizer. This indication is also corroborated by the approximately 10-fold reduction of photocurrents recorded with HBr with respect to AA present in comparable concentrations.

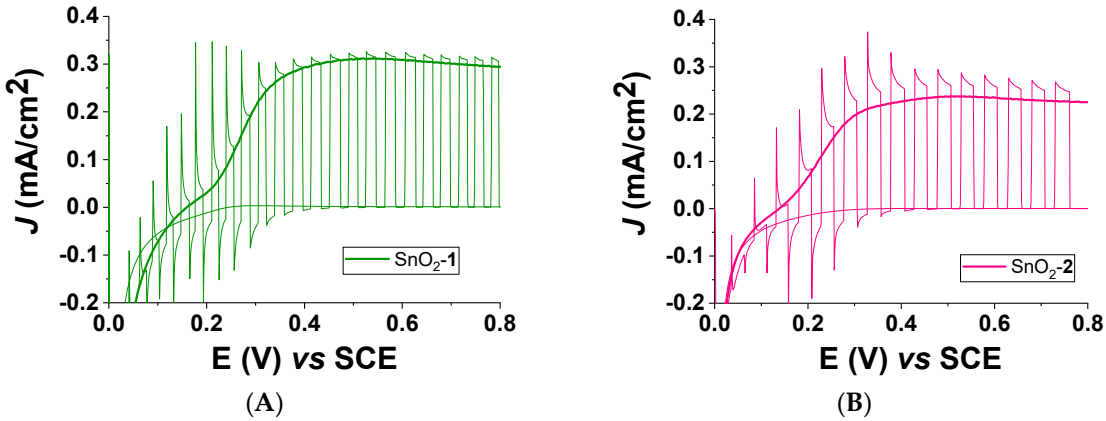

Figure 8. J/E curves of SnO_2-**1** (**A**) and SnO_2-**2** (**B**) photoanodes recorded in 0.1 M HBr (pH 1) under AM 1.5 G (0.1 W/cm^2) illumination through the FTO side.

The photoaction spectra (IPCE versus λ) recorded in 0.1 M HBr under 0.6 V versus SCE, a potential well into the plateau region of the respective J/E, are reported in Figure 9. Although maximum IPCE values are fairly small, with maximum values in the order of 2.5%, consistent with the modest photocurrents recorded under white light illumination, the photoaction spectra are in good agreement with the absorption profiles recorded on the sensitized thin films, testifying to the involvement of the excited state of each dye in the sensitization process. In particular, the photoaction spectra also point to the superiority of **1**, yielding higher photoconversion than **2** in correspondence of its broader B band with the added benefit of a red shifted response originating from Q band excitation extending up to 700 nm.

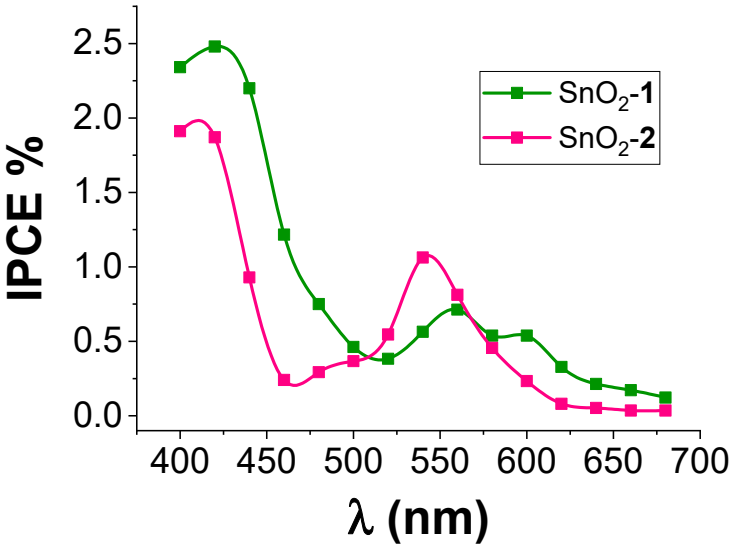

Figure 9. IPCE spectra of SnO_2-**1** and SnO_2-**2** photoanodes recorded in 0.1 M HBr (pH 1) under 0.6 V versus SCE applied bias. Illumination was through the ohmic contact (FTO).

The corresponding absorbed photon to current efficiencies (APCE or IQE (Inner Quantum Yield) = IPCE(λ)/LHE(λ) with LHE(λ) = $(1-10^{-A(\lambda)})$, where A(λ) is the photoelectrode absorbance at a given wavelength λ), have been calculated and reported and are shown in Figure S5. The APCE spectra are quite constant in the visible range with the best values again found with **1**, giving maximum values of approximately 3%, compared with less than 2.5% in the case of **2**. Despite the fact that different electronic states are populated by excitation in the respective Soret and Q bands, the consistency of the photoconversion values throughout the observed spectral range suggests that injection probably takes place from the lowest thermalized state of each porphyrin, indicating that injection could be under unfavourable kinetic competition with thermalization of the higher lying excited states.

3.5. Transient Absorption Spectroscopy

In order to specifically address charge separation dynamics, we performed nanosecond transient absorption spectroscopy (TAS) experiments on both the porphyrin dyes in solution and after their anchoring onto SnO_2 electrodes.

The photophysical behaviour of both porphyrins in 1:1 ethanol/toluene (5×10^{-4} M) was recorded after the ns-laser excitation at 532 nm and it tracks the characteristics of the dyes' excited states. Figure 10 reports the TAS obtained for **1** and **2** at different time delays with respect to the laser pulse.

Signals sampled at 0 delay are convolved with laser pulse, which in the presence of the amplifier impedance, has an instrumental response of approximately 300 ns. TAS taken at 0 delay, thus, still show in both cases features of the lowest singlet excited states (black line plus black squares) associated with the spontaneous emission, appearing as bleaching in the wavelength interval 600/700 nm. Such feature is quickly substituted by a weak and flat absorption extending from 600 to 800 nm and assigned to the lowest excited triplet (T_1) population, whose decay, being spin forbidden, occurs in a few microseconds (a weak ΔOD signal is still observable after 3 μs from the excitation (orange line)). The most prominent spectral feature of the triplet state is the presence of a strong absorption band centered around 500 nm (**1**) and 480 nm (**2**). For both dyes, the TAS spectra are in-line with previous findings, regarding other β-substituted porphyrins functionalized with donor/acceptor groups [37,38], as well as more symmetric structures [39], for which the lowest electronic states are mainly localized on the tetrapyrrolic ring, consistent with a small influence of the electron withdrawing branch in either the *meso* or β position of of the macrocycle on the electronic properties of the lowest excited states. When these dyes are adsorbed on SnO_2 in contact with 0.1 M $HClO_4$, the excited state leads

to the formation of a charge-separated (CS) state ($SnO_2(e^-)$-dye(h^+)). The CS state of porphyrin **1** (Figure 11A) is characterized, along with the ground state (Soret and Q-bands) bleaching, by the presence of a broad absorption band peaking at 730 nm and by the absence of the intense excited state absorption band at 500 nm, at least for a certain delay after the laser pulse. Indeed, spectra taken at 0 delay (Figure S6) are substantially convolved with the instrumental response, but still show features of the excited state, lacking the diagnostic 730 nm absorption band, which is offset by spontaneous emission. This indicates, at a qualitative level, incomplete quenching of the excited state by charge injection as a consequence of slow electron transfer rate from the excited dye to the semiconductor. Similar spectral features and dynamics are found with **2**, which compared to **1**, presents a narrower dye$^+$ absorption band, having its maximum at approximately 700 nm. In both cases, the CS state evolves slowly due to recapture of the photoinjected electrons with the oxidized dye and the transient signals do not recover completely within the timeframe of the experiment (3 ms), showing, in principle, a great potential for the exploitation of the long-lived CS state to drive redox reactions.

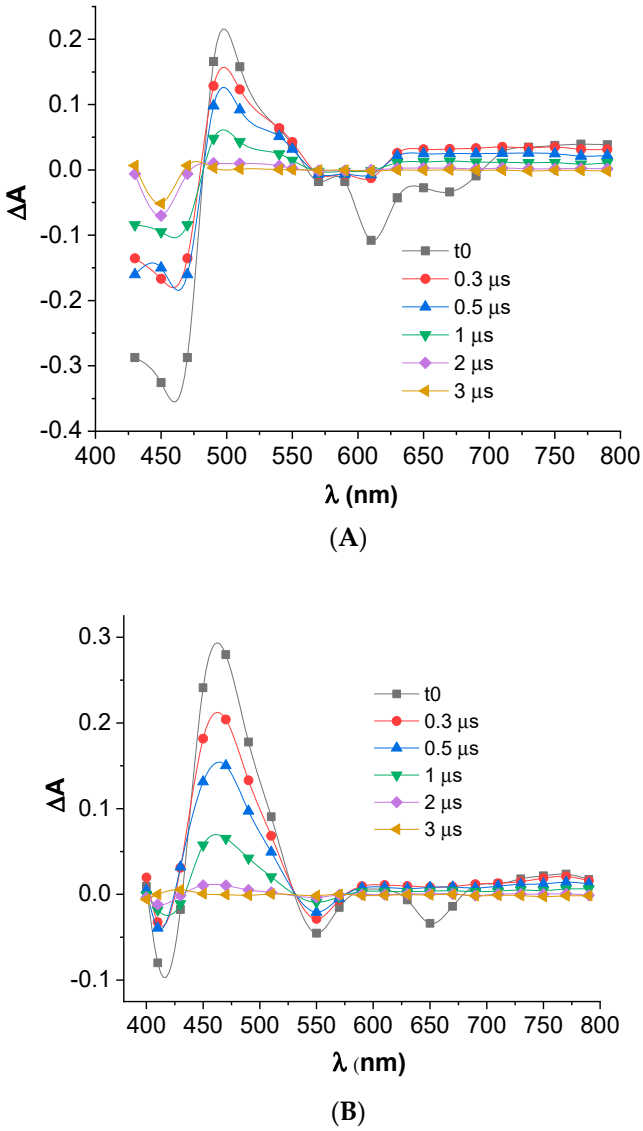

Figure 10. Transient absorption spectra of **1** (**A**) and **2** (**B**) at different delays from the 532 nm ns-laser excitation recorded in 1:1 EtOH/toluene; 350 Ω oscilloscope impedance.

Recombination kinetics of the CS state ($SnO_2(e^-)$-dye(h^+)) were monitored at 690 and 700 nm corresponding to the diagnostic CS absorption manifold of porphyrins **1** and **2**, respectively. In general,

the dynamics are multiexponential due to surface heterogeneity, with at least one fast component in the 0–2 ms interval, and a long component extending from 2 to 20 ms. Upon application of anodic potential, withdrawal of electrons, percolating through the SnO_2 network to the electron collector, occurs, reducing electron density within the sensitized film and slowing down, as a consequence, recapture by the oxidized dye, which in the presence of an inert electrolyte (0.1 M $HClO_4$), constitutes the only recombination pathway. As a result, both the initial amplitude of the CS state and that of the long component increase. Overall, upon 0.8 V versus Pt (approximately 0.5 V versus SCE) bias, approximately half of the initial population of the CS states survives after approximately 10 ms from the initial excitation (Figure 12 and Figure S7).

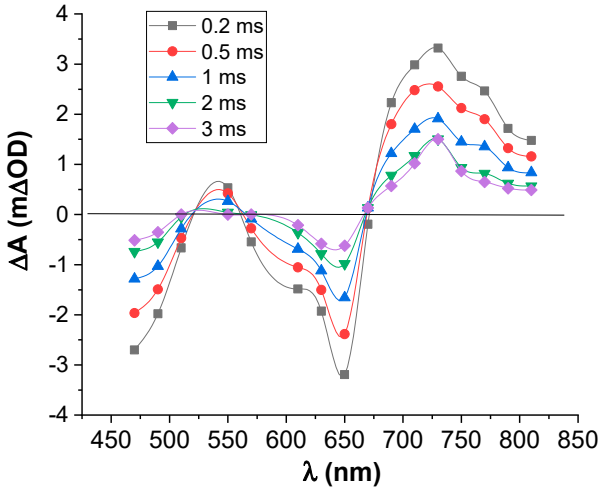

(**A**)

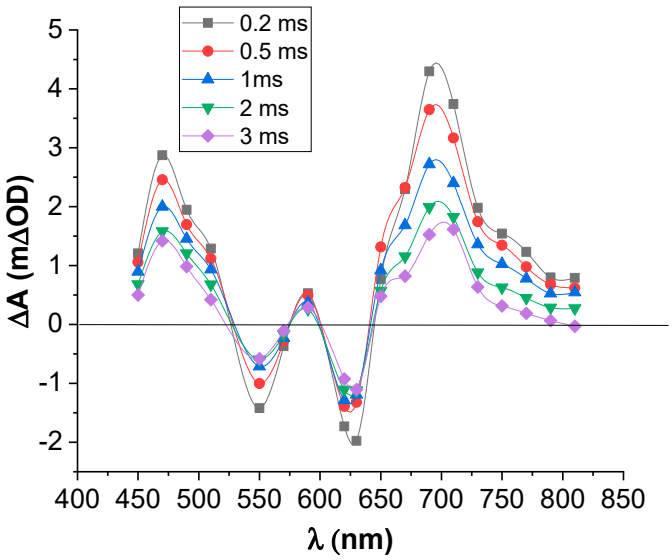

(**B**)

Figure 11. Transient absorption spectra of SnO_2-**1** (**A**) and SnO_2-**2** (**B**) at different delays from the 532 nm ns-laser excitation recorded at OCP in 0.1 M $HClO_4$; 1 MΩ oscilloscope resistance.

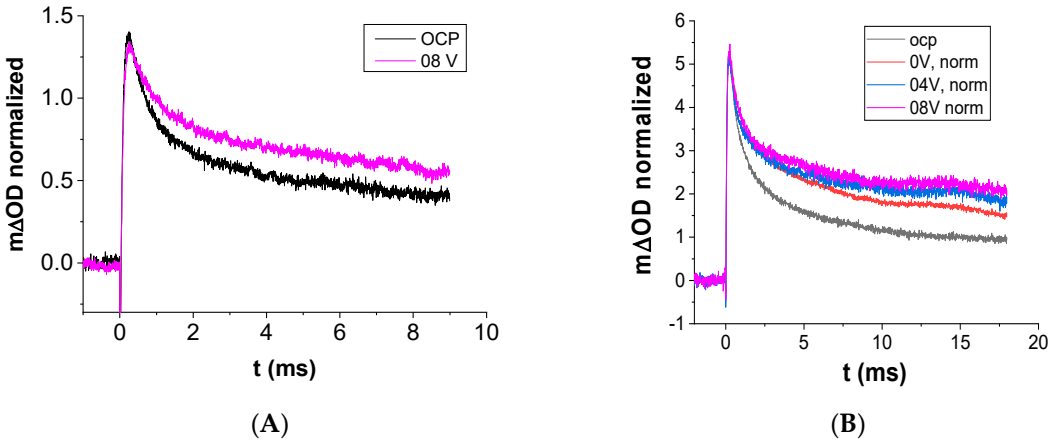

Figure 12. Kinetic evolution of $SnO_2(e^-)$-**1**(h^+) (**A**) and $SnO_2(e^-)$-**2**(h^+) (**B**). The charge-separated state was observed following ns laser excitation at 532 nm in 0.1 M $HClO_4$ at OCP (black line) and under different applied biases (values versus Pt); 1 MΩ oscilloscope resistance. (B) The traces have been normalized to the maximum ΔOD observed at 0.8 V versus Pt.

The dynamics in the presence of Br^- allow quantification of the regeneration efficiency of the porphyrins, i.e., the ability to produce Br_3^- and hydrogen. As a Br^- electrolyte, we used the 0.1 M HBr/0.3 M NaBr formulation to keep the pH constant (hence the flat band potential of the metal oxide photoanode), while introducing a total 0.4 M Br^-, which is in large excess with respect to the surface concentration of photoxidized dye. Nevertheless, even under such conditions, we observed the incomplete recovery of the ΔA traces (Figure 13), indicating that the electron transfer from Br^- to the oxidized dye was slow compared to recombination, partly explaining the small photocurrents and IPCE discussed before. In 0.4 M Br, the dependence of the transient kinetics on the applied bias was similar to that described before in the case of the blank electrolyte, confirming that recombination of photoinjected electrons with the oxidized dyes is still the dominant charge loss pathway, despite the presence of the electron donor (Figure S4). Pseudo-first-order regeneration and recombination rate constants evaluated at 0.8 V versus Pt, well within the plateau region (i.e., that corresponding to the maximum charge extraction rate from the sensitized SnO_2) of the J/E curves (Figure 8), were found to be 1.4 10^2 and 1.9 10^2 s^{-1} for **1** and 3.9 10^1 and 2.2 10^2 s^{-1} for **2**. This corresponds to regeneration efficiencies η_{reg} of the order of 40% for **1** and 15% for **2**. It should be considered that the evaluation based on $\tau_{1/2}$ is relatively rough, but is only available here since the time duration of decays exceed the current capabilities of our spectrometric apparatus to frame the complete time evolution of the recombination/regeneration kinetics. Nevertheless, the indication of a sluggish regeneration of the oxidized dye clearly emerges in both cases, and may contribute to explaining the better performance of **1** with respect to **2**. This latter trend is also consistent with the larger driving force for Br^- oxidation available to **1** (0.37 eV) with respect to **2** (0.3 eV) for Br^- oxidation (E^0 Br^-/Br_2 is 0.86 V versus SCE in water). In addition, when considering the elementary step in the monoelectronic oxidation of $Br^-/Br\cdot$(1.68 V versus SCE), the one that is likely to be followed at the molecular level in the sensitized photoanode [8], the driving force becomes clearly unfavorable to efficient regeneration, and only by working under sufficient Br^- concentration could one obtain a small overlap between the porphyrin$^+$ states and the redox electrolyte to observe some degree of charge transfer and Br_3^- formation.

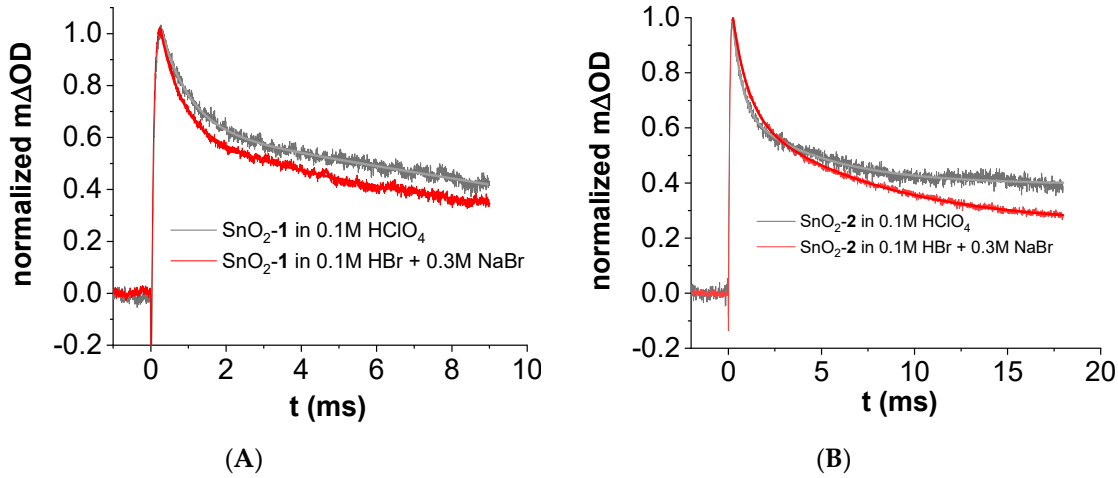

Figure 13. Kinetic evolution of $SnO_2(e^-)$-**1**(h^+) (**A**) and $SnO_2(e^-)$-**2**(h^+) (**B**) charge-separated states after the ns laser excitation at 532 nm in 0.1 M $HClO_4$ (black traces) and 0.1 M HBr + 0.3 M NaBr (red traces) under 0.8 V versus Pt applied bias; 1 MΩ oscilloscope resistance. Traces have been normalized for unity.

4. Conclusions

In this work, we have explored the electronic properties of fluorinated porphyrins intended to be applied in sensitized n-type PECs for HBr splitting. Thus, the effort was to increase the ground state oxidation potential of the dyes in order to access energy-demanding redox reactions, to obtain adsorption stability in an aqueous environment thanks to hydrophobic properties, and to provide the ability to bind metal oxides for photoinduced charge injection. These requirements led to the design of Zn(II) porphyrins, carrying either 4 or 5 *meso* pentafluorophenyl moieties as electron acceptor groups, and a further electron withdrawing branch inserted in either the β or *meso* position. The latter is tasked with binding the metal oxide, and with mediating the electronic coupling for charge injection from the excited state. DFT and TDDFT calculations showed that delocalization of the excited states on the electron withdrawing link was partially successful with the BTD electron acceptor, however the electronic density on the cyano-acrylic moiety remained comparatively small with respect to that localized in the ring. Nevertheless, in the presence of aqueous AA as a hole scavenger, the β design **1** was able to produce a 40% superior photocurrent with respect to the *meso* design **2**, ostensibly due to better injection and broader light harvesting. TA recorded on the sensitized photoanodes in contact with an inert electrolyte revealed indeed, in both cases, the formation of a long lived charge separated as a consequence of photoinduced injection, but the persistence of some unquenched emission at early delays indicated that injection was in neither cases optimal. Finally, both dyes could be successfully employed in the splitting of HBr, where red photons, up to 700 nm, could be harvested and converted, and again, **1** performed better than **2**, although the photoanodic current associated with such process was decreased by an approximately 10-fold factor with respect to the AA case. On the basis of TA results, the large drop photocurrent when Br^- was used as electron donor was ascribed to inefficient regeneration of the oxidized sensitizer as a result of insufficient driving force for Br^- oxidation. This study will, thus, serve as a guide for the development of better designs for dye-sensitized PECs, which may profit from the advantages and shortcomings outlined with these two model sensitizers.

Supplementary Materials: The following are available online at http://www.mdpi.com/2076-3417/9/13/2739/s1. Figure S1: Fluorescence decay of porphyrin 1 (A) and 2 (B) in toluene solution, bold black line (λ_{exc} = 442 nm; λ_{em} = 642 nm). Convolution fit, red line. Weighted residuals are shown under the decay curves. Figure S2: CV (**A**) and DPV (**B**) of porphyrin **1** on glassy carbon electrode, in DMF+0.1 M TBAP, at 0.2 $V{\cdot}s^{-1}$. Figure S3: CV (**A**) and DPV (**B**) of porphyrin **2** on glassy carbon electrode, in DMF+0.1 M TBAP, at 0.2 $V{\cdot}s^{-1}$. Figure S4: Net photocurrents (i.e., after the subtraction of the dark contribution) recorded for SnO_2-1 (**A**) and SnO_2-2 (**B**) photoanodes in 0.1 M HBr (pH 1) under 1 sun (0.1 mW/cm^2) AM 1.5 G illumination from both the back side of the

electrode (i.e., the FTO side) and the front side (i.e., from the electrolytic solution). Average curves of 5–7 electrodes are reported. Figure S5: APCE spectra of SnO_2-**1** (**A**) and SnO_2-**2** (**B**) photoanodes recorded in 0.1 M HBr (pH 1) under 0.6 V vs SCE applied bias. Illumination was through the FTO. Figure S6: Transient spectra of SnO_2-**1** (A) and SnO_2-**2** (B) photoanodes at OCP in 0.1 M $HClO_4$ as an inert electrolyte taken at 0 delay. Notice the apparent bleaching in the 600–750 region, due to spontaneous emission. Figure S7: Kinetic evolution of $SnO_2(e^-)$-**1**(h^+) (**A**–**B**) and $SnO_2(e^-)$-**2**(h^+) (**C**–**D**) charge separated states after the ns laser excitation at 532 nm in 0.1 M HBr + 0.3 M NaBr at OCP and under different applied biases (values vs Pt). 1 MΩ oscilloscope resistance. In (**B**) and (**D**) the traces have been normalized to unity. Table S1: Electrochemical energy levels of porphyrins **1** and **2**, referred to the ferrocenium/ferrocene redox couple.

Author Contributions: E.B., N.Z. and A.N. performed photoelectrochemical experiments. S.B. wrote part of the manuscript and interpreted data. F.T. wrote part of the manuscript and supervised the synthetic activity. A.O.B. and G.D.C. carried out dye preparation and characterization in solution. S.C. supervised research, interpreted results, wrote part of the manuscript and revised it. M.P. supervised the synthetic activity.

Acknowledgments: A.O.B., M.P., F.T., and G.D.C. gratefully acknowledge Regione Lombardia and Fondazione Cariplo 2014) for financial support and for the use of instrumentation purchased through the SmartMatLab Center project (Fondazione Cariplo Grant 2013-1766 and Giacomo Antifora for the help with the syntheses. G.D.C. greatly thanks the Università degli Studi di Milano (Piano Sostegno alla Ricerca 2018 LINEA A Azione A–Giovani Ricercatori) for financial support.

Conflicts of Interest: The authors declare no conflicts of interest.

References

1. Eisenberg, R.; Nocera, D. Overview of the Forum on Solar and Renewable Energy. *Inorg. Chem.* **2005**, *44*, 6799. [CrossRef] [PubMed]
2. Lewis, N.S.; Nocera, D.G. Powering the Planet: Chemical Challenges in Solar Energy Utilization. *Proc. Natl. Acad. Sci. USA* **2006**, *103*, 15729–15735. [CrossRef] [PubMed]
3. Lewis, N.S. Research Opportunities to Advance Solar Energy Utilization. *Science* **2016**, *103*, 1920. [CrossRef] [PubMed]
4. Tachibana, Y.; Vayssieres, L.; Durrant, J.R. Artificial Photosynthesis for Solar Water-Splitting. *Nat. Photonics* **2012**, *6*, 511–518. [CrossRef]
5. Ardo, S.; Sang, H.P.; Warren, E.L.; Lewis, N.S. Unassisted solar-driven photoelectrosynthetic HI splitting using membrane-embedded Si microwire arrays. *Energy Environ. Sci.* **2015**, *8*, 1484. [CrossRef]
6. Levy-Clement, C.; Heller, A.; Bonner, W.; Parkinson, B. Spontaneous Photoelectrolysis of HBr and HI. *J. Electrochem. Soc.* **1982**, *129*, 1701–1705. [CrossRef]
7. Khaselev, O.; Turner, J.A. Photoelectrolysis of HBr and HI Using a Monolithic Combined Photoelectrochemical/Photovoltaic Device. *Electrochem. Solid-State Lett.* **1999**, *2*, 310–312. [CrossRef]
8. Brady, M.D.; Sampaio, R.N.; Wang, D.; Meyer, T.J.; Meyer, G.J. Dye-Sensitized Hydrobromic Acid Splitting for Hydrogen Solar Fuel Production. *J. Am. Chem. Soc.* **2017**, *139*, 15612–15615. [CrossRef] [PubMed]
9. Berardi, S.; Cristino, V.; Canton, M.; Boaretto, R.; Argazzi, R.; Benazzi, E.; Ganzer, L.; Borrego Varillas, R.; Cerullo, G.; Syrgiannis, Z.; et al. Perylene Diimide Aggregates on Sb-Doped SnO2: Charge Transfer Dynamics Relevant to Solar Fuel Generation. *J. Phys. Chem. C* **2017**, *121*, 17737–17745. [CrossRef]
10. Cho, K.T.; Tucker, M.C.; Ding, M.; Ridgway, P.; Battaglia, V.S.; Srinivasan, V.; Weber, A.Z. Cyclic Performance Analysis of Hydrogen/Bromine Flow Batteries for Grid-Scale Energy Storage. *ChemPlusChem* **2015**, *80*, 402–411. [CrossRef]
11. Brady, M.D.; Troian-Gautier, L.; Sampaio, R.N.; Motley, T.C.; Meyer, G.J. Optimization of Photocatalyst Excited—And Ground-State Reduction Potentials for Dye-Sensitized HBr Splitting. *ACS Appl. Mater. Interfaces* **2018**, *10*, 31312–31323. [CrossRef] [PubMed]
12. Mussini, P.R.; Orbelli Biroli, A.; Tessore, F.; Pizzotti, M.; Biaggi, C.; Di Carlo, G.; Lobello, M.G.; De Angelis, F. Modulating the electronic properties of asymmetric push–pull and symmetric Zn(II)-diarylporphyrinates with para substituted phenylethynyl moieties in 5,15 meso positions: A combined electrochemical and spectroscopic investigation. *Electrochim. Acta* **2012**, *85*, 509–523. [CrossRef]
13. Hodge, J.A.; Hill, M.G.; Gray, H.B. Electrochemistry of Nonplanar Zinc(II) Tetrakis(Pentafluorophenyl)porphyrins. *Inorg. Chem.* **1995**, *34*, 809–812. [CrossRef]
14. Yang, S.I.; Seth, J.; Strachan, J.P.; Gentemann, S.; Kim, D.; Holten, D.; Lindsey, J.S.; Bocian, D.F. Excited State Electronic Properties of Halogenated Tetraarylporphyrins. Tuning the Building Blocks for Porphyrin-Based Photonic Devices. *J. Porphyr. Phthalocyanines* **1999**, *3*, 117. [CrossRef]

15. Yella, A.; Lee, H.-W.; Tsao, H.N.; Yi, C.; Chandiran, A.K.; Nazeeruddin, M.K.; Diau, E.W.-G.; Yeh, C.-Y.; Zakeeruddin, S.M.; Grätzel, M. Porphyrin-sensitized solar cells with cobalt (II/III)–based redox electrolyte exceed 12 percent efficiency. *Science* **2011**, *334*, 629–634. [CrossRef] [PubMed]
16. Xie, Y.; Tang, Y.; Wu, W.; Wang, Y.; Liu, J.; Li, X.; Tian, H.; Zhu, W.-H. Porphyrin Cosensitization for a Photovoltaic Efficiency of 11.5%: A Record for Non-Ruthenium Solar Cells Based on Iodine Electrolyte. *J. Am. Chem. Soc.* **2015**, *137*, 14055–14058. [CrossRef] [PubMed]
17. Moore, G.F.; Blakemore, J.D.; Milot, R.L.; Hull, J.F.; Song, H.; Cai, L.; Schmuttenmaer, C.A.; Crabtree, R.H.; Brudvig, G.W. A visible light water-splitting cell with a photoanode formed by codeposition of a high-potential porphyrin and an iridium water-oxidation catalyst. *Energy Environ. Sci.* **2011**, *4*, 2389–2392. [CrossRef]
18. Materna, K.L.; Jiang, J.; Regan, K.P.; Schmuttenmaer, C.A.; Crabtree, R.H.; Brudvig, G.W. Optimization of Photoanodes for Photocatalytic Water Oxidation by Combining a Heterogenized Iridium Water-Oxidation Catalyst with a High-Potential Porphyrin Photosensitizer. *ChemSusChem* **2017**, *10*, 4526. [CrossRef]
19. Ronconi, F.; Syrgiannis, Z.; Bonasera, A.; Prato, M.; Argazzi, R.; Caramori, S.; Cristino, V.; Bignozzi, C.A. Modification of Nanocrystalline WO_3 with a Dicationic Perylene Bisimide: Applications to Molecular Level Solar Water Splitting. *J. Am. Chem. Soc.* **2015**, *137*, 4630–4633. [CrossRef]
20. Gritzner, G. Polarographic half-wave potentials of cations in nonaqueous solvents. *Pure Appl. Chem.* **1990**, *62*, 1839–1858. [CrossRef]
21. Gritzner, G.K.; Kůta, J. Recommendations on reporting electrode potentials in nonaqueous solvents: Iupac commission on electrochemistry. *Electrochim. Acta* **1984**, *29*, 869–873. [CrossRef]
22. Ronconi, F.; Santoni, M.-P.; Nastasi, F.; Bruno, G.; Argazzi, R.; Berardi, S.; Caramori, S.; Bignozzi, C.A.; Campagna, S. Charge injection into nanostructured TiO_2 electrodes from the photogenerated reduced form of a new Ru(II) polypyridine compound: The "anti-biomimetic" mechanism at work. *Dalton Trans.* **2016**, *45*, 14109. [CrossRef] [PubMed]
23. Frisch, M.J.; Trucks, G.W.; Schlegel, H.B.; Scuseria, G.E.; Robb, M.A.; Cheeseman, J.R.; Scalmani, G.; Barone, V.; Mennucci, B.; Petersson, G.A.; et al. *Gaussian 09, Revision A.02*; Gaussian, Inc.: Wallingford, CT, USA, 2009.
24. Prampolini, G.; Ingrosso, F.; Segalina, A.; Caramori, S.; Foggi, P.; Pastore, M. Dynamical and Environmental Effects on the Optical Properties of an Heteroleptic Ru(II)–Polypyridine Complex: A Multilevel Approach Combining Accurate Ground and Excited State QM-Derived Force Fields, MD and TD-DFT. *J. Chem. Theory Comput.* **2019**, *15*, 529–545. [CrossRef] [PubMed]
25. Tian, L.; Feiwu, C. Multiwfn: A multifunctional wavefunction analyzer. *J. Comput. Chem.* **2012**, *33*, 580–592. [CrossRef]
26. Lindsey, J.S.; Schreiman, I.C.; Hsu, H.C.; Kearney, P.C.; Marguerettaz, A. Rothemund and Adler-Longo Reactions Revisisted: Synthesis of Tetraphenylporphyrins under Equilibrium Conditions. *J. Org. Chem.* **1987**, *52*, 827–836. [CrossRef]
27. Di Carlo, G.; Orbelli Biroli, A.; Pizzotti, M.; Tessore, F.; Trifiletti, V.; Ruffo, R.; Abbotto, A.; Amat, A.; De Angelis, F.; Mussini, P.R. Tetraaryl ZnII Porphyrinates Substituted at β-Pyrrolic Positions as Sensitizers in Dye-Sensitized Solar Cells: A Comparison with Meso-Disubstituted Push-Pull ZnII Porphyrinates. *Chem. Eur. J.* **2013**, *19*, 10723. [CrossRef] [PubMed]
28. Golf, H.R.A.; Reissig, H.U.; Wiehe, A. Regioselective Nucleophilic Aromatic Substitution Reaction of Meso-Pentafluorophenyl-Substituted Porphyrinoids with Alcohols. *Eur. J. Org. Chem.* **2015**, *7*, 1548. [CrossRef]
29. Kolb, H.C.; Finn, M.G.; Sharpless, K.B. ChemInform Abstract: Click Chemistry: Diverse Chemical Function from a Few Good Reactions. *ChemInform* **2001**, *40*, 2004–2021. [CrossRef]
30. Covezzi, A.; Orbelli Biroli, A.; Tessore, F.; Forni, A.; Marinotto, D.; Biagini, P.; Di Carlo, G.; Pizzotti, M. 4D-π-1A type β-substituted ZnII-porphyrins: Ideal green sensitizers for building-integrated photovoltaics. *Chem. Commun.* **2016**, *52*, 12642–12645. [CrossRef]
31. Di Carlo, G.; Orbelli Biroli, A.; Pizzotti, M.; Tessore, F. Efficient sunlight harvesting by A4 β-pyrrolic substituted ZnII-porphyrins: A mini-review. *Front. Chem.* **2019**, *7*, 177. [CrossRef]
32. Gouterman, M.; Wagnière, G.H.; Snyder, L.C. Spectra of porphyrins: Part II. Four orbital model. *J. Mol. Spectrosc.* **1963**, *11*, 108–127. [CrossRef]
33. Archer, M.D. *Nanostructured and Photoelectrochemical Systems for Solar Photon Conversion*; Archer, D.M., Nozik, A.J., Eds.; Imperial College Press: London, UK, 2008; Volume 3.

34. Bergeron, B.V.; Marton, A.; Oskam, G.; Meyer, G.J. Dye-Sensitized SnO2 Electrodes with Iodide and Pseudohalide Redox Mediators. *J. Phys. Chem. B* **2005**, *109*, 937–943. [CrossRef] [PubMed]
35. Alibabaei, L.; Sherman, B.D.; Norris, M.R.; Brennaman, M.K.; Meyer, T.J. Visible photoelectrochemical water splitting into H2 and O2 in a dye-sensitized photoelectrosynthesis cell. *Proc. Natl. Acad. Sci. USA* **2015**, *112*, 5899–5902. [CrossRef] [PubMed]
36. Sheridan, M.V.; Wang, Y.; Wang, D.; Troian-Gautier, T.; Dares, C.J.; Sherman, B.D.; Meyer, T.J. Light-Driven Water Splitting Mediated by Photogenerated Bromine. *Angew. Chem. Int. Ed.* **2018**, *57*, 3449. [CrossRef] [PubMed]
37. Di Carlo, G.; Caramori, S.; Trifiletti, V.; Giannuzzi, R.; De Marco, L.; Pizzotti, M.; Orbelli Biroli, A.; Tessore, F.; Argazzi, R.; Bignozzi, C.A. Influence of Porphyrinic Structure on Electron Transfer Processes at the Electrolyte/Dye/TiO2 Interface in PSSCs: A Comparison between meso Push–Pull and β-Pyrrolic Architectures. *ACS Appl. Mater. Interfaces* **2014**, *6*, 15841–15852. [CrossRef] [PubMed]
38. Di Carlo, G.; Caramori, S.; Casarin, L.; Orbelli Biroli, A.; Tessore, F.; Argazzi, R.; Oriana, A.; Cerullo, G.; Bignozzi, C.A.; Pizzotti, M. Charge Transfer Dynamics in β- and Meso-Substituted Dithienylethylene Porphyrins. *J. Phys. Chem. C* **2017**, *121*, 18385–18400. [CrossRef]
39. Kim, D.; Holten, D.; Gouterman, M. Evidence from picosecond transient absorption and kinetic studies of charge-transfer states in copper(II) porphyrins. *J. Am. Chem. Soc.* **1984**, *106*, 2793–2798. [CrossRef]

© 2019 by the authors. Licensee MDPI, Basel, Switzerland. This article is an open access article distributed under the terms and conditions of the Creative Commons Attribution (CC BY) license (http://creativecommons.org/licenses/by/4.0/).